PCCP

RSC Publishing

PAPER

Towards understanding the electronic structure of Fe-doped CeO₂ nanoparticles with X-ray spectroscopy

Wei-Cheng Wang,[ab] Shih-Yun Chen,[c] Per-Anders Glans,[b] Jinghua Guo,[b] Ren-Jie Chen,[cd] Kang-Wei Fong,[c] Chi-Liang Chen,[e] Alexandre Gloter,[f] Ching-Lin Chang,*[a] Ting-Shan Chan,[d] Jin-Ming Chen,[d] Jyh-Fu Lee[d] and Chung-Li Dong*[d]

This study reports on the electronic structure of Fe-doped CeO₂ nanoparticles (NPs), determined by coupled X-ray absorption spectroscopy and X-ray emission spectroscopy. A comparison of the local electronic structure around the Ce site with that around the Fe site indicates that the Fe substitutes for the Ce. The oxygen K-edge spectra that originated from the hybridization between cerium 4f and oxygen 2p states are sensitive to the oxidation state and depend strongly on the concentration of Fe doping. The Ce $M_{4,5}$-edges and the Fe $L_{2,3}$-edges reveal the variations of the charge states of Ce and Fe upon doping, respectively. The band gap is further obtained from the combined *absorption–emission* spectrum and decreased upon Fe doping, implying Fe doping introduces vacancies. The oxygen vacancies are induced by Fe doping and the spectrum reveals the charge transfer between Fe and Ce. Fe^{3+} doping has two major effects on the formation of ferromagnetism in CeO₂ nanoparticles. The first, at an Fe content of below 5%, is that the formation of Fe^{3+}–Vo–Ce^{3+} introduces oxygen deficiencies favoring ferromagnetism. The other, at an Fe content of over 5%, is the formation of Fe^{3+}–Vo–Fe^{3+}, which favors antiferromagnetism, reducing the Ms. The defect structures Fe^{3+}–Vo–Ce^{3+} and Fe^{3+}–Vo–Fe^{3+} are crucial to the magnetism in these NPs and the change in Ms can be described as the effect of competitive interactions of magnetic polarons and paired ions.

Introduction

CeO₂ is one of the most important rare-earth metal oxides and has a wide range of industrial applications, such as in catalysis[1,2] and solid oxide fuel cells.[3,4] The electronic structure and chemical and physical properties of CeO₂ can be easily altered by introducing oxygen vacancies. Such defects can be rapidly formed and eliminated, giving rise to localized or delocalized 4f electron states. Another potentially important application is the diluted magnetic oxides with Curie temperature above room temperature which are a new class for spintronics. Magnetic ordering in a semiconductor depends on a small proportion of transition metal ion dopants that have partially filled d shells, which allow the unpaired electron to mediate ferromagnetism.[5–9] Many other mechanisms have also been suggested. They include the second-phase or exchange interaction.[10–12] The discovery of room temperature ferromagnetism (RTFM) in undoped hafnium dioxide thin films was quite unexpected since neither Hf^{4+} nor O^{2-} are magnetic ions, and the d and f shells of the Hf^{4+} ion are either empty or full. The origin of the RTFM in such a material has been suggested to be the oxygen vacancy defects and RTFM has been described as the mutual interaction of magnetic polarons.[13,14] Since then, more studies of dilute magnetic semi-conductors and oxides have been conducted. In materials with defect-induced magnetism, the advanced nanostructuring technique can be used to artificially engineer and control the defects, such that nanostructured materials are good model systems for investigating the origin of ferromagnetism. Ferromagnetism has been proposed to be a universal phenomenon in nanoparticles of extremely small size,[15,16] but its mechanism is not well understood. Chen *et al.* recently elucidated the relationship between defects and ferromagnetism in CeO₂ nanocrystals.[17] The ferromagnetism of such nanocrystals can be enhanced by adding non-magnetic trivalent dopants, and this effect is attributable to the formation of more oxygen vacancies.[18] In the same manner, the introduction

[a] *Department of Physics, Tamkang University, Tamsui, 25137, Taiwan.*
    E-mail: clchang@mail.tku.edu.tw

[b] *Advanced Light Source, Lawrence Berkeley National Laboratory, Berkeley,*
    California 94720, USA

[c] *Department of Material Science and Engineering,*
    National Taiwan University of Science and Technology, Taipei, Taiwan

[d] *National Synchrotron Radiation Research Center, Hsinchu, 30076, Taiwan.*
    E-mail: dong.cl@nsrrc.org.tw

[e] *Institute of Physics, Academia Sinica, Taipei 11529, Taiwan*

[f] *Laboratoire de Physique des Solides, Université Paris Sud, CNRS UMR 8502,*
    F-91405 Orsay, France

This journal is © the Owner Societies 2013

Phys. Chem. Chem. Phys., 2013, **15**, 14701–14707 | **14701**

of Fe dopant, which normally has a valence of less than +4, may alter the crystal structure and the valence of the Ce ions, changing the chemical or physical properties. The electronic structures around the Ce and Fe sites provide valuable information. Therefore, this study examines the electronic structure of Fe-doped CeO_2 NPs at room temperature using X-ray absorption spectroscopy (XAS) and X-ray emission spectroscopy (XES), which can directly probe the occupied and unoccupied states near the Fermi level, to reveal the effect of Fe doping on the defects and electronic structure of CeO_2 nanoparticles.

Experimental

CeO_2 nanoparticles were prepared by the precipitation method. $Ce(NO_3)_3 \cdot 6H_2O$ was mixed with 80% EG/water with stirring at 600 rpm at room temperature. When the precursor had totally dissolved, NH_4OH (3 mol L^{-1}) was added. The solution was maintained at 60 °C for 21 h. The precipitate was separated by centrifugation at 6000 rpm for 15 min and then washed several times using DI water and alcohol. After it was dried for 24 h, CeO_2 NPs were obtained. To form the Fe-doped CeO_2 NPs, in the first step, the precursor $Fe(NO_3)_3 \cdot 6H_2O$ was added at the same time as $Ce(NO_3)_3 \cdot 6H_2O$ that was mixed with EG/water. The NPs were characterized using synchrotron X-ray diffraction (XRD) performed at BL01C2 of the National Synchrotron Radiation Research Center (NSRRC), Taiwan. The concentrations of Fe-doped CeO_2 were 1%, 3%, 5%, 7%, 9% and 11%, and the size of the NPs varied from 2 nm to 3 nm. The O K-edge soft-X-ray emission and soft-X-ray absorption spectroscopy experiments were performed at undulator beamline 7.0.1 at the Advanced Light Source (ALS), Lawrence Berkeley National Laboratory (LBNL). The soft-X-ray emission spectra were obtained using a high-resolution grazing incidence grating Rowland circle-type spectrometer with a two-dimensional multi-channel plate detector whose resolution was set to 0.5 eV. Soft-X-ray absorption at the Ce $M_{4,5}$-edges was conducted at BL7.0.1 at ALS. The resolution was set to 0.2 eV for the soft-X-ray absorption measurements. The extended X-ray absorption fine structure (EXAFS) measurements at the Ce L_3-edge and the Fe K-edge were made at Wiggler beamline 17 C using the transmission mode at the NSRRC. The monochromator Si (111) crystals were used in Wiggler beamline 17 C with a resolving power $E/\Delta E$ of better than 7000. Since the energy of the Ce L_2-edge is about 6164 eV, the energy range over which EXAFS measurements of the Ce L_3-edge are made is usually extended to 400 eV above the L_3-edge (5723 eV). The soft X-ray absorption spectra at Fe $L_{2,3}$-edges were recorded at the HSGM bending magnet beamline 20 A in the total electron yield mode with an energy resolution of 0.2 eV.

Results and discussion

Fig. 1(a) presents the powder X-ray diffraction patterns of Fe-doped CeO_2 NPs with various Fe doping concentrations (from 1% to 11%) and undoped CeO_2 NPs. The diffraction peaks are indexed according to the cubic fluorite structure with
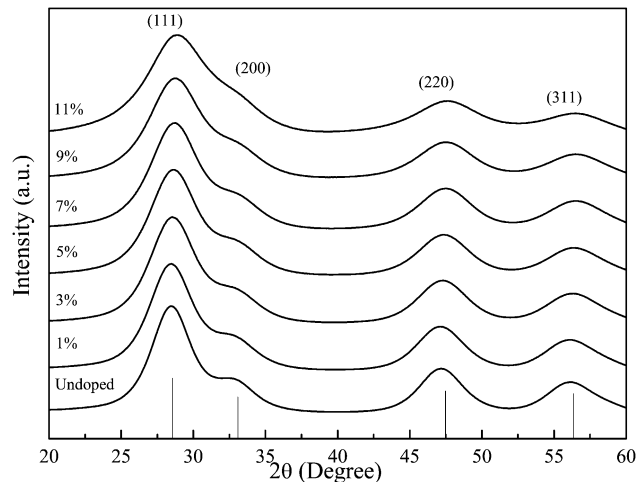

Fig. 1 (a) XRD results for pure CeO_2 NPs and those doped with various concentrations (from 1% to 11%) of Fe.

the space group $Fm31m$ (JCPDS 34-0394), which is that of bulk CeO_2. No diffraction peak from any impurity, such as pure Ce and Fe, or any other cerium oxide or iron oxide, was obtained within the detection limit. The peaks broadened as the Fe doping level increased. Several possibilities can explain the peak broadening, especially the decreasing particle size and distorted structure. The mean particle size can be estimated from the full width at half maximum of the XRD peaks based on the Scherrer equation. The particle size was estimated to be in the range from 2 to 3 nm, which is consistent with the TEM results. The diffraction peaks of Fe-doped CeO_2 were shifted to high angles relative to those of the undoped oxide, indicating the reduction of the lattice constant upon doping with Fe. This reduction is attributable to the substitution of the smaller Fe^{3+} (0.064 nm) for the Ce^{4+} (0.097 nm) ions, and suggests that Fe ions are incorporated into the CeO_2 matrix. Although the XRD results demonstrate the absence of a secondary phase or Fe metal clusters, direct identification of local impurity clusters that do not exhibit long-range order may depend on EXAFS.

Unlike XRD, EXAFS is applicable to short-range ordered structural phases. The short-range structural information that is provided by EXAFS offers element-specific insight, which is complementary to that provided by XRD, and includes information about the number, position and identity of atoms that surround absorbing elements, as well as about structural disorder. To provide information about local atomic structures, Fig. 2(a) and (b) display the Fourier-transformed amplitude of the Ce L-edge (k range 3.1 to 10.1 Å^{-1}) and Fe K-edge (k range 3.04 to 12.1 Å^{-1}) EXAFS oscillations of CeO_2 NPs with various Fe doping concentrations together with the Fe K-edge of Fe metal, FeO and Fe_2O_3 for reference. The radial distribution functions in Fig. 2(a) and (b) provide partial atomic distribution around the Ce and Fe sites. The dominant Fourier-transformed intensity in Fig. 2(a) and (b) is provided by the scattering from the first coordination shell, respectively, corresponding to Ce–O pair and Fe–O pair. The first coordination peak of the Fe-doped samples in the Fourier-transformed EXAFS signal in Fig. 2(b),
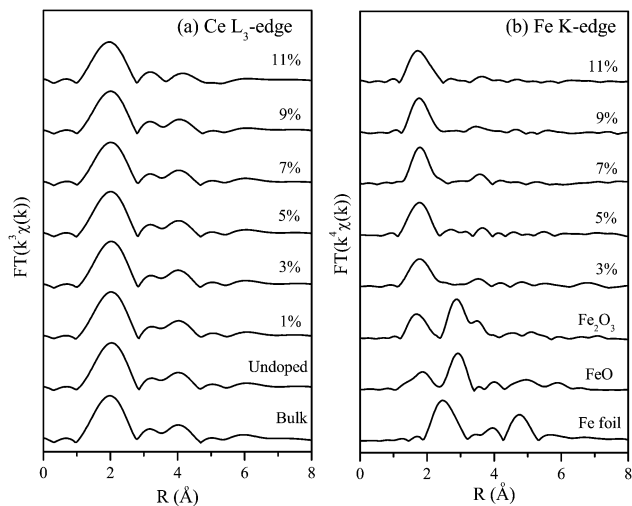
Fig. 2 Fourier-transformed amplitude of EXAFS at (a) Ce L_3-edge and (b) Fe K-edge.

viewed from an Fe atom, differs from that of the reference samples (Fe metal and Fe oxides), but resembles that in Fig. 2(a), viewed from a Ce atom. This fact implies that Fe atoms substitute for Ce ions in the CeO_2 matrix. The Fourier-transformed EXAFS results also reveal that the concentrations of impurities, such as Fe metal clusters or Fe oxides, in the doped samples are too low to be detected, such that these impurities can be neglected herein.

Fig. 3(a) displays the oxygen K-edge XAS spectra of CeO_2 bulk, NPs and NPs with various concentrations of Fe dopants (from 1% to 11%). All spectra are normalized to the energy of 565 eV, at which the electrons transition to the continuum states. The feature-rich spectra of the O K-edge arise from the transitions from the O 1s to the 2p-derived unoccupied states.
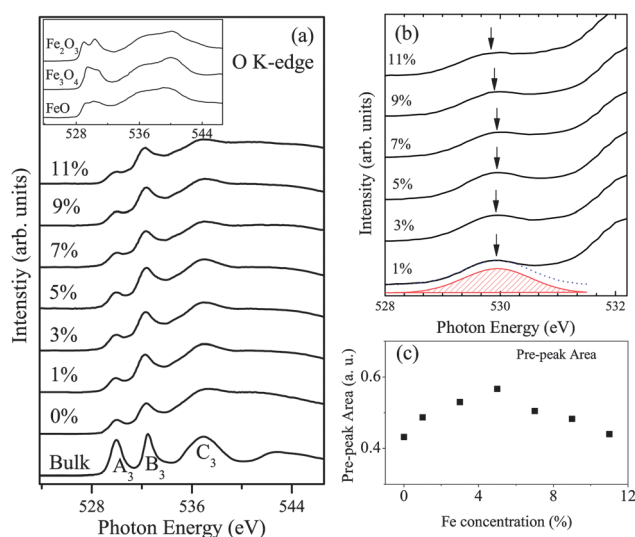

Fig. 3 (a) O K-edge XAS of CeO_2 bulk, NPs and NPs with different Fe concentrations (1% to 11%). (b) Enlargement of the pre-edge region. The red area at the bottom is fitted with a Gaussian function, from which is determined the amount of Ce 4f–O 2p hybridized states. (c) Variation of the intensity of peak A_3.

The spectra of the iron oxides are plotted in the inset for reference to compare the hybridizations of Ce 4f–O 2p and Fe 3d–O 2p. The spectra of three reference iron oxides (FeO, Fe_2O_3, and Fe_3O_4) demonstrate that the two peak structures at 529–531 eV are hybridized with O 2p and Fe 3d-t_{2g} and 3d-e_g states. The peak positions of cerium dioxides differ markedly from those of iron oxides, implying that the formation of iron oxide in these nanoparticles is unlikely. The spectral profiles of Fe-doped CeO_2 nanoparticles resemble those of bulk CeO_2, except that the features are broadened, indicating that the electronic structure and the crystal structure of the nanoparticles are similar to those of CeO_2. The broadening of the features originated in the modulation of the electronic structure by the Fe doping. Cerium dioxides yield three peaks (A_3, B_3 and C_3) at 530, 532.5 and 537 eV, as displayed in Fig. 3(a). Peaks A_3, B_3 and C_3 reflect the hybridization of the empty O 2p hole states with the cerium-dominated 4f, 5d-e_g and 5d-t_{2g} states, respectively.[19] Notably, a comparison of the bulk and nanoparticle samples reveals crystal field effects, as the separation of the energies of the 5d-e_g and 5d-t_{2g} states of the nanoparticles exceeds that of the bulk sample. The crystal field effects are less important in doped and undoped nanoparticles since the separation of energy seems to be only weakly sensitive to the Fe content of the material. Additionally, the intensity of peak A_3 varied upon doping with Fe. The variation of this peak intensity implies a change in the hybridization of the O 2p–Ce 4f states, and so reflects the 4f occupancy number and the valence of Ce.[19] The decreased intensity of peak A_3 of nanoparticles relative to the bulk suggests a reduction of the unoccupied 4f states, which may indicate that the 4f orbital in nanoparticles is filled with electrons. Since the formation of oxygen vacancies may pull down the energy of the Ce d and f orbitals closer to the Fermi level,[20,21] the energy shift is related to the shift of the d and f states of the Ce atoms down in energy toward the Fermi level, such that some of the f states even cross E_f, lowering the valence of the Ce ions. Hence, the drop in the intensity of A_3 may reflect the fact that the nanoparticles contain more oxygen vacancies than the bulk. To elucidate the variation of the intensity of peak A_3, a Gaussian function was fitted to it,[22] as shown in Fig. 3(b). For all nanoparticles with various Fe doping levels, the changes in peak A_3 clearly reveal the following. First, the energy of the peak shifts upward with the concentration of Fe dopant up to a certain concentration, beyond which it shifts back to low energy upon further increase in the dopant concentration. Second, the area under the peak increases with the doping level up to 5% and declines beyond 5%, as plotted in Fig. 3(c). These results demonstrate that the 4f occupancy varied with doping concentration.

Owing to the large overlap of the wave functions of O 2p and the Ce 4f orbital, the pre-edge of the O K-edge that arises from the O 2p–Ce 4f states may yield the density of Ce 4f states. However, the Ce $M_{4,5}$-edge XAS corresponds to the electron transition from the Ce $3d_{3/2}$ and $3d_{5/2}$ core levels into the 4f unoccupied electronic states. It thus directly reflects the occupancy of the 4f orbital. Fig. 4(a) presents the Ce $M_{4,5}$-edge XAS of Fe-doped CeO_2 nanoparticles along with the reference samples
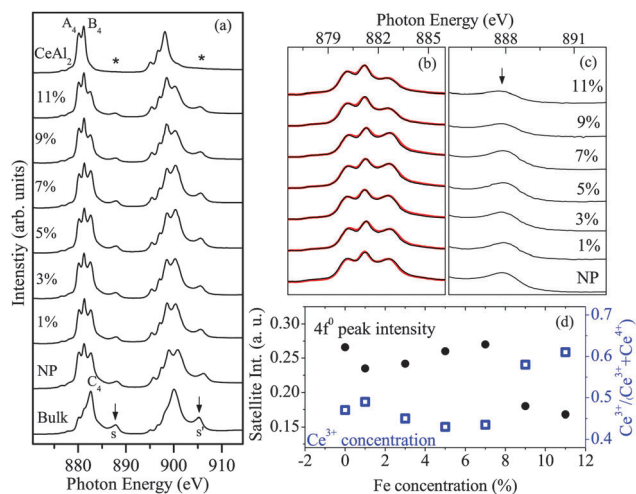
Fig. 4 (a) Ce $M_{4,5}$-egde XAS of CeO_2 NPs with various Fe contents (1% to 11%) and of reference samples that contain trivalent and tetravalent Ce. (b) Enlargement of experimental (black line) M_5-edge and that fitted (red line) by linear combination of CeO_2 and $CeAl_2$ spectra. (c) Enlargement of the $4f^0$ satellite feature. (d) Comparison of intensities of satellite features and $Ce^{3+}/(Ce^{3+} + Ce^{4+})$ ratios.

$CeAl_2$ and CeO_2. Bulk CeO_2 yields two distinct satellite structures s and s′ (indicated by arrows) ∼5 eV above the main M_5- and M_4-edges. However, these satellite structures are smeared out in the nanoparticles and absent from $CeAl_2$ (indicated by an asterisk). The Ce in $CeAl_2$ and CeO_2 is typically regarded as trivalent and tetravalent, respectively. Normally, the M_4-edge follows the M_5-edge and is regarded as a replica of the M_5-edge. For simplicity, only the M_5-edge is considered below. The bulk CeO_2 yields a dominant peak C_4 at 882.6 eV with a significant satellite structure s ∼5 eV above it. $CeAl_2$ exhibits double peaks A_4 and B_4 at lower energies (880.2 and 881.2 eV) without the satellite structure. At first glance, all nanoparticles exhibit mixed Ce^{3+} and Ce^{4+} configurations in their ground states, as the spectral profiles include the characteristic features of $CeAl_2$ and CeO_2. Further inspection demonstrates that the intensity ratio of $(A_4 + B_4)$ to C_4 varies with the concentration of Fe doping. The intensity of feature $(A_4 + B_4)$ initially increases as the size of the material declines from the bulk to NPs, implying an increase in the Ce^{3+} contribution,[23] and feature $(A_4 + B_4)$ becomes slightly weaker as the doping level approaches 5%, but it eventually increases again as the doping level rises above 5%. A standard procedure was used to evaluate the Ce^{3+}/Ce^{4+} ratio.[24] The combined spectra of $CeAl_2$ and CeO_2 were utilized to examine the valence state of Ce. Fig. 4(b) shows an enlargement of the M_5-edge and the results of the best fits (red curves) to the experimental data (black curves). Fig. 4(d) displays the resulting $Ce^{3+}/(Ce^{3+} + Ce^{4+})$ intensity ratios. The satellite structures s and s′ originate from transitions to the 4f states in the conduction band[25] and thus they are indicative of the contribution of $4f^0$ states. Since trivalent $CeAl_2$ yields no such satellite peak, the intensity of the satellite peak can be used to determine the amount of $4f^0$ states. Fig. 4(c) magnifies the region of the satellite and its contribution is extracted by fitting a peak function.

Fig. 4(d) also plots the variation of the density of $4f^0$ states *versus* the proportion of Fe dopant. The area under the peak increases with doping up to 5–7%, and then decreases as the doping level increases further. The change in $4f^0$ intensity is consistent with the Ce^{3+} proportion that was estimated from the M-edge (blue square) in Fig. 4(d). Accordingly, the dependence of the valence on the concentration of the doping level can be divided into two regions: (I) at a dopant concentration below 5–7%, the amount of trivalent Ce decreases as the dopant level increases, and (II) at a dopant concentration above 5–7%, the amount of trivalent Ce increases with the dopant level. This observation agrees closely with the O K-edge result obtained above.

The relationship between Ce valence and defects was established using various oxygen vacancy engineering processes in CeO_2 nanoparticles.[17,26,27] In pure CeO_2 nanoparticles, the amount of trivalent Ce increased with the number of oxygen vacancies that were formed. In the Cr-doped nanoparticles, the Cr dopants retained the 3+ oxidation state at various doping levels. The proportion of Ce^{3+} was enhanced by Cr^{3+} doping since the addition of Cr^{3+} creates more oxygen defects than were present in pure CeO_2 nanoparticles. Herein, the observed behavior is more complex than in Cr-doped nanoparticles, as the valence of Ce does not vary monotonically with the Fe doping level. The defect structures and local electronic structures around the Fe sites are essential for elucidating this extraordinary phenomenon. Generally, an impurity may be present as a defect level slightly below the conduction band or slightly above the valence band, and so influence the electronic structure and band edge around the E_f. Fig. 5(a) shows the absorption–emission spectra, which reflect information about not only the band gap but also the electronic structure in CB and VB near the Fermi level. The band gap is observed between the CB maximum and the VB minimum, which can be determined by the first-order derivatives of the
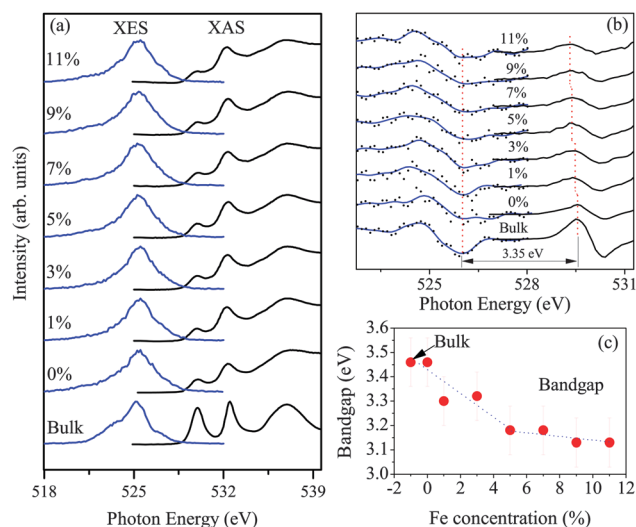

Fig. 5 (a) O K-edge X-ray *absorption–emission spectrum*. (b) First-order derivative of XAS and XES spectra for bandgap determination. (c) Bandgap *versus* Fe concentration.

absorption and emission spectra, respectively.[28] Fig. 5(b) displays the differential *absorption–emission* spectrum of bulk CeO_2, which yields a fundamental band-gap energy of 3.35 eV. This value is close to the band gap that is measured by the UV-visible absorption spectrum.[29] Fig. 5(c) plots the variation of the band gap with the doping level of Fe in CeO_2 nanoparticles.

The band gap of nanoparticles is narrower than that of bulk CeO_2, and this narrowing can be attributed to the modulation of 4f electronic states. Clearly, the pre-peak of the O K-edge, whose structure originates from O 2p–Ce 4f hybridization, has a lower intensity in nanoparticles than in the bulk because nanoparticles contain more oxygen vacancies and therefore more Ce^{3+} ions. The change in the electronic configuration from Ce^{4+} ($4f^0$) to Ce^{3+} ($4f^1$) implies the entry of an extra electron into the 4f orbital, and this orbital filling reduces the energy gap. Notably, when Fe was doped into the CeO_2 nanoparticles, the band gap decreased up to a doping level $\sim$5–7%. As Fe doping rose above 5–7%, the band gap continuously but slowly narrowed. Several factors influence the band gap of a material. The quantum size effect is well known to enlarge the band gap (by, for example, shifting the conduction band to a higher energy and the valence band to a lower energy). The quantum size effect may not be significant herein since the sizes of the nanoparticles are in the narrow range of $\sim$2–3 nm. This finding is consistent with the observation of Masui *et al.*, who found no quantum size effect in ultrafine CeO_2 particles of at least 2.6 nm in size.[30] Additionally, if this effect were dominant, then the bandgap would be higher in nanoparticles, rather than low. Consequently, the size effect does not dominate the change in the band gap. The difference between the electronegativities of oxygen and the metallic element has been also suggested to affect the bandgap[31,32] in a binary semiconductor system. A larger difference between the electronegativities of the oxygen and the metal should result in a larger band gap. In Fe-doped CeO_2, Fe has a higher electronegativity (1.81) than does Ce (1.12), so the band gap in Fe-doped CeO_2 should be larger than that in undoped CeO_2. However, this fact does not fully explain the observed differences between the band gaps. In the doped system, the dopant may induce a defect level within the band gap of the host material and thereby reduce the band gap.[33] The band gap herein monotonically decreases with increasing Fe concentration, and this effect is contrary to the mutually consistent O K-edge and Ce M-edge results. The most likely cause of the change in the band gap is the difference between the defect structures associated with oxygen vacancies in these nano-scaled particles as a function of Fe doping.[34] Since the oxygen vacancies are derived from doping, the electronic structure and the defect structure around the Fe sites might have been critical.

Fig. 6 presents the Fe $L_{2,3}$-edge XAS of Fe-doped CeO_2 nanoparticles, which exhibits the transitions from Fe $2p_{1/2}$ and $2p_{3/2}$ to Fe 3d unoccupied states. The inset plots the results for the samples FeO, Fe_2O_3 and Fe_3O_4 for reference. The peak positions and the spectral line shape of the 3d metal L-edge depend strongly on the local atomic and electronic structures of the metal ions, providing information on the electronic
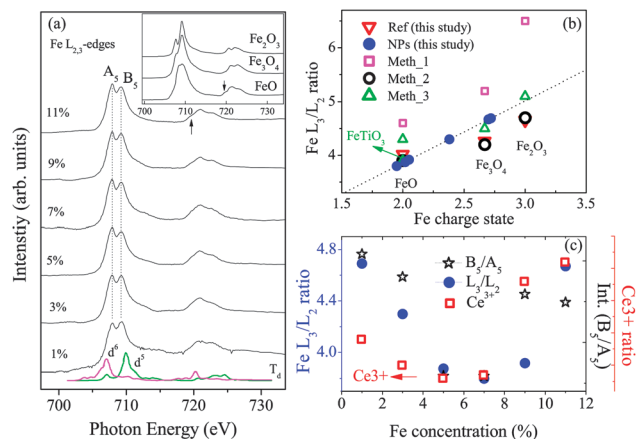

Fig. 6 (a) Fe $L_{2,3}$-edge of XAS of CeO_2 NPs with different concentrations of Fe; the inset shows the results for FeO, Fe_2O_3 and Fe_3O_4. (b) Fe charge state against the L_3/L_2 ratio. (c) Correlation among the Fe L_3/L_2 ratio, the A_5/B_5 intensity ratio and the $Ce^{3+}/(Ce^{3+} + Ce^{4+})$ ratio.

configuration and valence states. With respect to the reference samples, the iron in FeO and Fe_2O_3 has octahedral symmetry, as revealed by the double peak profiles, and their d orbitals split into lower energy t_{2g} and higher energy e_g states. Fe_3O_4 yields three prominent features at 706.5, 708 and 709.2 eV, which correspond to Fe^{2+} at the O_h sites, Fe^{3+} at the T_d sites, and Fe^{3+} at the O_h sites, respectively. In the nanoparticles, the tetrahedral coordination of the CeO_2 matrix and the electric interaction cause the d orbital of the iron to exhibit three- and two-fold degeneracy, corresponding to the lower two e_g states and the higher three t_{2g} states. The spectral profiles of Fe-doped CeO_2 NPs are similar to each other and differ from those of FeO (Fe^{2+}), Fe_3O_4 (mixed Fe^{2+} and Fe^{3+}), and Fe_2O_3 (Fe^{3+}). The difference between the intensities of the t_{2g} and e_g peaks is indicative of the variation of the Fe 3d-occupancy.[35] Direct comparison of the specific multiplet structures at the L_3- and L_2-edges enables the charge states of these NPs and the reference samples to be determined. Feature A_5 is attributed to Fe^{2+} and that at B_5 is attributed to Fe^{3+}. According to the calculated spectra of Fe^{2+} and Fe^{3+} in T_d and O_h coordination environments, all Fe L-edge line shapes are consistent with a tetrahedral coordination,[36] which is expected when Fe ions are substituted for Ce in the CeO_2 matrix. The bottom of Fig. 6(a) displays the calculated XAS (taken from ref. 36) of Fe^{2+} and Fe^{3+} under T_d symmetry with 10Dq = 2 eV. The XAS spectra of trivalent Fe ions in iron oxides are well known to include only doublet peaks at both L_2 and L_3 edges. Fe_2O_3 yields a dominant peak close to 710 eV, along with double peaks near 721 and 723 eV, which are characteristic of Fe^{+3} ions. The small peak at 719.8 eV is characteristic of Fe^{2+} ions. All Fe-doped CeO_2 nanoparticles yield this small feature, which verifies the mixed valence of Fe.

The experimental observation of the changes in e_g and t_{2g} can be explained in terms of d orbital occupancy. The valence state can be estimated by the specific weight of each of the two lines, as the ratio $I(L_3)/I(L_2)$. Fig. 6(b) presents the relative intensities of the white lines evaluated using different methods

that have been described elsewhere (Method 1: FeO 4.6(0.3), Fe_3O_4 5.2(0.3), Fe_2O_3 6.5(0.3); Method 2: FeO 3.9(0.3), Fe_3O_4 4.2(0.3), Fe_2O_3 4.7(0.3); Method 3: FeO 4.3(0.2), Fe_3O_4 4.5(0.1), Fe_2O_3 5.1(0.3)[37,38]) Although the values obtained from different reports vary, $I(L_3)/I(L_2)$ universally increases with the valence state. Fig. 6(b) plots the $I(L_3)/I(L_2)$ of the nanoparticles and reference samples herein. These values are consistent with the universal trend, and the Fe valences of the nanoparticle samples herein (indicated by solid blue circles) are between those of Fe^{2+} and Fe^{3+}. Fig. 6(c) plots the $I(L_3)/I(L_2)$ ratio against dopant concentration. Since feature A_5 is attributed to Fe^{2+} and the one at B_5 to Fe^{3+} components, the valence of iron can be determined from the intensity of peaks A_5 and B_5. It is consistent with the trend of $I(L_3)/I(L_2)$, which is displayed in Fig. 6(c). As revealed by Ce M-edge and O K-edge, the valence of Ce initially increases and then decreases with increasing doping, as also presented in Fig. 6(c). The Ce valence therefore varies oppositely to the Fe valence, suggesting that charge transfer may occur between Ce and Fe. With respect to the magnetic measurements of the Fe-doped NPs,[39] the variation of Ms with the Fe concentration is consistent with earlier studies by Wen et al.,[40] although the maximum Ms value obtained herein is 5%, whereas Wen et al. obtained a maximum Ms at 3%. Ms increases with Fe doping concentration up to 5% because the dopant produces oxygen vacancies (Vo), strongly supporting the F-center mediated exchange mechanism, in which an Vo traps an electron to form an F-center, which constitutes a bound magnetic polaron.[41] However, as the Fe concentration rises over 5%, Ms decreases; a mechanism other than the magnetic polaron mechanism appears to be involved, influencing the magnetic behavior of NPs with a high concentration of dopants. Based on the above results, although more oxygen vacancies are formed as the Fe concentration increases over 5%, the decrease in Ms is attributable to the formation of TM paired ions. The paired TM ions are expected to exhibit a superexchange interaction with each other that is mediated by one oxygen ion, giving rise to antiferromagnetic behavior and reducing the Ms value.

Conclusion

The electronic and atomic structures of CeO_2 nanoparticles with various concentrations of dopant Fe were investigated by X-ray absorption and X-ray emission spectroscopy. As the dopant Fe content is varied, two regions are identified: at lower doping, vacancies are formed by the Fe doping and so the Ms increased. This effect is explained by the interaction of magnetic polarons. The defect structure that is formed by Fe in this region is thought to be Fe^{3+}–Vo–Ce^{3+} and the increase in Fe^{2+} and Ce^{4+} contents was attributed to the charge transfer between the Ce and Fe. However, at a higher doping level, the vacancies still can be created by the Fe doping – but at a low rate. In this region, Ms decreases with increasing dopant concentration. The charge transfer between Ce and Fe is insignificant and so the Fe^{3+} and Ce^{3+} concentrations increase. Consequently, the number of Fe^{3+}–Vo–Fe^{3+} defect structures is increased, causing the paired ion structure. The paired ions mediated by one oxygen ion are expected to give rise to antiferromagnetism, such that the Ms decreases as the doping level increases. The major effect of doping CeO_2 nanoparticles with Fe^{3+} is the formation of different defect structures, causing a competitive interaction between ferromagnetism (caused by magnetic polarons) and antiferromagnetism (caused by paired ions).

Acknowledgements

References

1 C. T. Campbell, *Science*, 2005, **309**, 713–714.
2 F. Esch, S. Fabris, L. Zhou, T. Montini, C. Africh, P. Fornasiero, G. Comelli and R. Rosei, *Science*, 2005, **309**, 4.
3 S. R. Bishop, H. L. Tuller, Y. Kuru and B. Yildiz, *J. Eur. Ceram. Soc.*, 2011, **31**, 2351–2356.
4 Z. Zhan, *Science*, 2005, **308**, 844–847.
5 H. Ohno, *Science*, 1998, **281**, 951–956.
6 Y. Ohno, D. K. Young, B. Beschoten, F. Matsukura, H. Ohno and D. D. Awschalom, *Nature*, 1999, **402**, 3.
7 B. Beschoten, P. A. Crowell, I. Malajovich, D. D. Awschalom, F. Matsukura, A. Shen and H. Ohno, *Phys. Rev. Lett.*, 1999, **83**, 4.
8 Y. Matsumoto, *Science*, 2001, **291**, 854–856.
9 T. Dietl, *Science*, 2000, **287**, 1019–1022.
10 A. Singhal, S. N. Achary, J. Manjanna, S. Chatterjee, P. Ayyub and A. K. Tyagi, *J. Phys. Chem. C*, 2010, **113**, 9.
11 H. S. Hsu, J. C. A. Huang, Y. H. Huang, Y. F. Liao, M. Z. Lin, C. H. Lee, J. F. Lee, S. F. Chen, L. Y. Lai and C. P. Liu, *Appl. Phys. Lett.*, 2006, **88**, 242507.
12 G. Venkataiah, M. R. S. Huang, H. L. Su, C. P. Liu and J. C. A. Huang, *J. Phys. Chem. C*, 2010, **114**, 6.
13 M. Venkatesan, C. B. Fitzgerald and J. M. D. Coey, *Nature*, 2004, **430**, 1.
14 J. Coey, M. Venkatesan, P. Stamenov, C. Fitzgerald and L. Dorneles, *Phys. Rev. B: Condens. Matter Mater. Phys.*, 2005, **72**, 024450.
15 A. Sundaresan and C. N. R. Rao, *Nano Today*, 2009, **4**, 96–106.
16 A. Sundaresan, R. Bhargavi, N. Rangarajan, U. Siddesh and C. Rao, *Phys. Rev. B: Condens. Matter Mater. Phys.*, 2006, **74**, 161306.
17 S.-Y. Chen, C.-H. Tsai, M.-Z. Huang, D.-C. Yan, T.-W. Huang, A. Gloter, C.-L. Chen, H.-J. Lin, C.-T. Chen and C.-L. Dong, *J. Phys. Chem. C*, 2012, **116**, 8707–8713.
18 S.-Y. Chen, K.-W. Fong, T.-T. Peng, C.-L. Dong, A. Gloter, D.-C. Yan, C.-L. Chen, H.-J. Lin and C.-T. Chen, *J. Phys. Chem. C*, 2012, **116**, 26570–26576.

19 J. A. Rodriguez, J. C. Hanson, J.-Y. Kim, G. Liu, A. Iglesias-Juez and M. FernaÂndez-GarcõÂa, *J. Phys. Chem. B*, 2003, **107**, 9.

20 Y. Q. Song, H. W. Zhang, Q. Y. Wen, H. Zhu and J. Q. Xiao, *J. Appl. Phys.*, 2007, **102**, 043912.

21 H.-T. Chen and J.-G. Chang, *J. Phys. Chem. C*, 2011, **115**, 14745–14753.

22 S. Banerjee, T. Hemraj-Benny, M. Balasubramanian, D. A. Fischer, J. A. Misewich and S. S. Wong, *ChemPhysChem*, 2004, **5**, 1416–1422.

23 S. Kucheyev, B. Clapsaddle, Y. Wang, T. van Buuren and A. Hamza, *Phys. Rev. B: Condens. Matter Mater. Phys.*, 2007, **76**, 235420.

24 L. A. J. Garvie and P. R. Buseck, *J. Phys. Chem. Solids*, 1999, **60**, 5.

25 R. Karnatak, J. Esteva, H. Dexpert, M. Gasgnier, P. Caro and L. Albert, *Phys. Rev. B: Condens. Matter Mater. Phys.*, 1987, **36**, 1745–1749.

26 N. J. Lawrence, J. R. Brewer, L. Wang, T.-S. Wu, J. Wells-Kingsbury, M. M. Ihrig, G. Wang, Y.-L. Soo, W.-N. Mei and C. L. Cheung, *Nano Lett.*, 2011, **11**, 2666–2671.

27 P. Dutta, S. Pal, M. S. Seehra, Y. Shi, E. M. Eyring and R. D. Ernst, *Chem. Mater.*, 2006, **2006**, 3.

28 C. X. Kronawitter, J. R. Bakke, D. A. Wheeler, W.-C. Wang, C. Chang, B. R. Antoun, J. Z. Zhang, J. Guo, S. F. Bent, S. S. Mao and L. Vayssieres, *Nano Lett.*, 2011, **11**, 3855–3861.

29 S. Sathyamurthy, K. J. Leonard, R. T. Dabestani and M. P. Paranthaman, *Nanotechnology*, 2005, **16**, 1960–1964.

30 T. Masui, K. Fujiwara, K. Machida and G. Adachi, *Chem. Mater.*, 1997, **9**, 2197–2204.

31 F. D. Quarto, C. Sunseri, S. Piazza and M. C. Romano, *J. Phys. Chem. B*, 1997, **101**, 7.

32 J. B. Goodenough, *Czech. J. Phys.*, 1967, **17**, 33.

33 N. Serpone, *J. Phys. Chem. B*, 2006, **110**, 7.

34 Y. Yalçın, M. Kılıç and Z. Çınar, *Appl. Catal., B*, 2010, **99**, 469–477.

35 P. A. v. Aken, B. Liebscher and V. J. Styrsa, *Phys. Chem. Miner.*, 1998, **25**, 5.

36 G. v. d. Laan and I. W. Kirkman, *J. Phys: Condens. Matter*, 1992, **4**, 16.

37 C. Colliex, T. Manoubi and C. Ortiz, *Phys. Rev. B: Condens. Matter Mater. Phys.*, 1991, **44**, 11402–11411.

38 H. K. Schmid and W. Mader, *Micron*, 2006, **37**, 426–432.

39 T. T. Peng, S.-Y. Chen, C.-L. Chen, Y. Y. Peng, K.-W. Fong, C.-L. Dong, W.-C. Wang, T.-S. Chan, J.-M. Chen, J.-F. Lee, H.-J. Lin, C.-T. Chen, A. Gloter, C.-L. Chang and J. Guo, to be submitted, 2013.

40 Q.-Y. Wen, H.-W. Zhang, Q.-H. Yang, Y.-Q. Song and J. Q. Xiao, *J. Appl. Phys.*, 2010, **107**, 09C307.

41 J. M. D. Coey, M. Venkatesan and C. B. Fitzgerald, *Nat. Mater.*, 2005, **4**, 173–179.